

Stress-Corrosion Cracking Behavior of AISI-409 Welded with a filler metal flux cored AWS E316LT1-4

Eduardo Miguel da Silva^a, Ricardo Luiz Perez Teixeira^{b*} , Sebastião Carlos da Costa^b,
Edmilson Otoni Corrêa^b , Rosinei Batista Ribeiro^c

^aUniversidade Federal de São João del-Rei, São João del-Rei, MG, Brasil.

^bUniversidade Federal de Itajubá, Itajubá, MG, Brasil.

^cCentro Universitário Teresa D'Ávila, Lorena, SP, Brasil.

Received: September 24, 2023; Revised: May 20, 2024; Accepted: June 01, 2024

Ferritic stainless steel is essential in many industries due to its corrosion resistance advantages over austenitic stainless steels. However, it is susceptible to embrittlement caused by factors such as grain growth, sigma phase formation, and carbide precipitation. This study investigates the stress corrosion cracking (SCC) behavior of AISI-409 ferritic stainless steel welded with AWS E316LT1-4 flux-cored wire, with heat inputs ranging from 400 J/mm to 805 J/mm. SCC tests were conducted by applying a constant load, followed by mechanical and microstructural analysis upon failure. Interestingly, higher heat input exhibited superior SCC resistance despite slower cooling rates compared to lower heat input. SCC initiated in the heat-affected zone (HAZ) and extended into the ferritic region. Photomicrographs depicted a ductile-to-brittle transition with reduced elongation values. Two distinct fracture regions were observed: dimples and cleavage facets, indicative of SCC-induced brittle fracture behavior. These findings provide insights into the SCC behavior of ferritic stainless steel, guiding the development of more resilient, corrosion-resistant materials for various industries.

Keywords: Ferritic stainless steel, stress corrosion cracking, welding.

1. Introduction

Stress corrosion cracking (SCC) occurs when a susceptible material, typically passive alloys, is subjected to applied tensile stress or residual stress and exposed to a corrosive environment¹⁻⁴. This phenomenon has been a major issue in welded joints of austenitic stainless steels used in environments containing chlorides at elevated temperatures. Such catastrophic failures occur in crucial industries, including the chemical and petrochemical industries⁵⁻⁹.

In general, stress corrosion cracking leads to crack formation at stress levels below the yield stress of the material, typically well below the design tension and fatigue limit of a structural component¹⁰⁻¹³. Consequently, resistance to SCC becomes a critical requirement when welding austenitic stainless steel. However, SCC is significantly influenced by metallurgical phenomena occurring during welding or post-welding heat treatments¹⁴⁻¹⁷.

While austenitic stainless steel is more susceptible to SCC, ferritic steel types can also be prone to this corrosive phenomenon. In this context, engineering has played a prominent role in developing techniques and consumables for welding ferritic steels with austenitic stainless steels. The goal is to combine the low resistance to stress corrosion cracking found in austenitic stainless steel with the high thermal conductivity of ferritic steel and the good weldability of austenitic stainless steel¹⁸⁻²⁰.

According to Jeong et al.²¹, the most crucial characteristic in selecting stainless steel for a given application is its resistance to corrosion, along with considerations of strength, ductility, weldability, cost, and other factors. Austenitic stainless steels offer the best combination of mechanical properties and corrosion resistance but come at a higher manufacturing cost, primarily due to the elevated price of nickel. Therefore, these factors have driven the development and utilization of ferritic stainless steels applications, especially where corrosion resistance, such as stress corrosion, is paramount. Ferritic stainless steels, with their higher Cr / C ratio, exhibit better corrosion resistance than martensitic stainless steels²².

Ferritic stainless steels find extensive application in exhaust systems, piping, and high-temperature equipment. However, exposure to elevated temperatures promotes the precipitation of intermetallic phases, compromising their mechanical properties (ductility and toughness) and corrosion resistance. Welding these materials must address two primary challenges: sensitization (formation of chromium carbides - Cr₂₃C₆), which can reduce corrosion resistance, and irreversible grain growth, leading to crack formation during solidification and loss of mechanical properties in the heat-affected zone.

To combat sensitization, alloying elements that reduce carbon's effect on chromium carbide formation, combined with controlled thermal cycles, are employed. In the case of grain growth, minimizing heat input through appropriate

*e-mail: ricardo.luiz@unifei.edu.br

welding conditions is crucial to mitigate harmful effects and excessive deformation.

In this context, precise control of metal transfer during welding is of paramount importance. Among various modes, pulsed welding stands out as an economically viable choice for flux-cored arc welding. Compared to the short-circuit transfer mode, the pulsed mode offers an increased deposition rate, typically around 10 to 15% higher^{23,24}. Additionally, pulsed mode promotes grain refinement in the heat-affected zone and offers better heat control, essential for stainless steel welding.

However, optimizing pulse parameter settings can be challenging. Research in the literature has focused on achieving higher arc stability under these conditions. This study aims to investigate the influence of heat input on the susceptibility of ferritic stainless steel AISI-409 during flux-cored arc welding using AWS E316LT1-4. The research explores the phenomenon of stress corrosion cracking (SCC) in an aqueous solution containing 43% MgCl₂ and includes mechanical and microstructural characterization of the welded joint.

1.1. Microstructural characterization

It is widely recognized that a dependable method for predicting the microstructure of weld metal involves the use of the Schaeffer diagram. This diagram, depicted in Figure 1, considers the influence of both austenite formers and ferrite formers, represented by numerical factors in the calculations of chromium equivalent (Cr_{eq}) and nickel equivalent (Ni_{eq}). The diagram aligns with the conditions outlined in this research, wherein it was welded a ferritic stainless steel base metal with a flux-cored filler metal composed of austenitic steel. Prior investigations conducted by Lopes et al.²⁵, Hajiannia et al.²⁶, and Sundaresan²⁷, have established that the maximum attainable dilution is 30%, a value that was adopted in this study. Consequently, it is crucial to emphasize that the weld metal contains approximately 10% delta ferrite, which possesses the potential to harden due to martensite formation.

In various applications, the presence of delta ferrite at certain levels has proven advantageous in weld metals. It acts as a beneficial component that mitigates or eliminates the susceptibility to hot cracking within the fusion welding zone during solidification. Delta ferrite achieves this by

facilitating the dissolution of substances such as sulfur and phosphorus, thereby preventing their segregation at grain boundaries within the weld metal. Such segregation could serve as initiation points for cracks, which might be exacerbated by the inherent stresses induced during welding processes²⁸.

Conversely, a substantial content of martensitic formation can potentially lead to hydrogen-induced cracking, a phenomenon akin to what is observed in carbon steels with a carbon content exceeding 0.45% by weight. However, limited data in the literature confirm this phenomenon in the context of ferritic stainless steels. Furthermore, martensite is identified as a potential contributor to material weakness, which could initiate fracture formation in the base material. It is important to note that the likelihood of martensite formation increases with higher cooling rates resulting from reduced heat input during welding tests. Interestingly, according to Lopes et al.²², a combination of martensitic microstructure and ferrite enhances toughness when compared to a fully ferritic structure.

2. Materials and Experimental Procedure

To achieve the objectives set forth in this study, experimental conditions based on a Pulsed Flux Cored Arc Welding Process were employed. The samples, made of AISI 409 ferritic stainless steel, had dimensions of 130 mm × 65 mm × 3 mm, and were configured with a butt joint, single-V groove, and flat position. An austenitic stainless-steel flux-cored filler metal classified as AWS E316LT1-4 (specifically, ESAB OK TUBRIGHT 316L), featuring a diameter of 1.2 mm, was utilized. The chemical compositions of the steel samples and filler metal are detailed in Table 1.

The welding equipment used was an Inversal 300 multi-process power supply, as shown in Figure 2, with Digital control and operation set in the current imposition mode for the pulsed transfer (1) by maintaining a fixed welding voltage during the tests²⁹. The welding torch (2) was attached to an MC-46 device (Welding car), which allowed a control of its speed of movement in the flat position (3) For the attachment of the specimens and protection of the root of the joint, a system with movable fasteners (4), coupled to a bracket, was used to allow the protection of the root of the welding by inserting an inert gas (argon), fed with a controlled flow rate. The length of the wire consumed in each test, as well as the welding time, was evaluated with the aid of a tachometer coupled to a wire speed meter (MVA-1) (5). The shielding gas flow rate was kept constant during the welding process, and it was recorded on the VGA flow meter (6).

The shielding gas consisted of an Argon-CO₂ mixture (75% Ar + 25% CO₂) at a flow rate of 14 l/min. The distance between the contact tip and the workpiece was maintained at 22.5 mm. The welding setup comprised a digital welding power supply, with a welding gun mounted on a mechanical tractor for controlled positioning. Welding deposition was carried out using reverse polarity (DC+) at a fixed voltage level of 23 V.

The pulsed welding parameters employed in this research, including peak current (I_p), peak time (t_p), base current (I_b), and frequency (f), were predetermined based on previously optimized welding conditions established by Dias³⁰. These parameters are detailed in Table 2. To achieve varying heat inputs, the travel speed (v_s) was adjusted within the range of 22 to 44.3 cm/min.

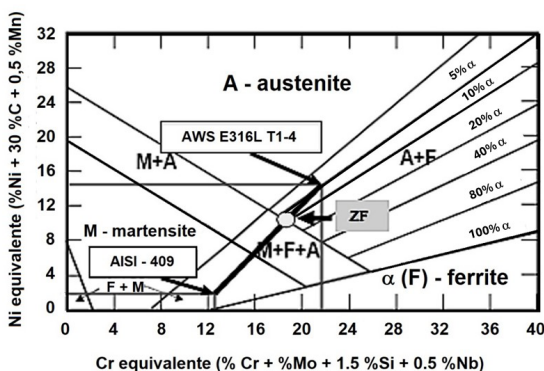


Figure 1. Schaeffer diagram for the welded joint of AISI 409 with filler metal of flux-cored wire AWS E316LT1-4.

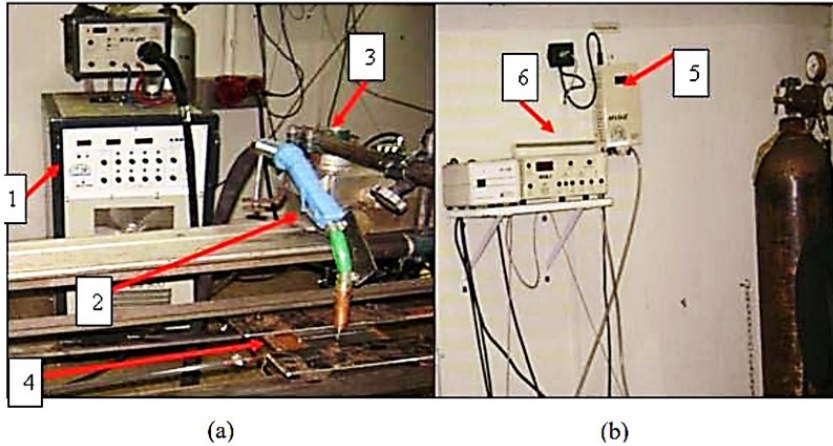


Figure 2. Welding test bench. (a) Experimental set-up; (b) System of Gas flow measurement and wire feeding.

Table 1. Chemical composition (%in weight) of the ferritic stainless steel AISI-409 and flux cored arc welding AWSE316LT1-4.

	C	Si	Mn	Cr	Ni	P	S	N	Ti	Nb	Mo
	%	%	%	%	%	%	%	%	%	%	%
AISI-409	0.03	1.00	1.00	10.50-11.70	0.50	0.04	0.02	0.030	6xC-0.75	0.17	-
AWS 316LT1-4	0.03	1.00	1.58	18.5	12.4	-	-	-	-	-	2.46

Table 2. Experimental welding condition.

Experiments	Ip (A)	tp (ms)	Ib (A)	tb (ms)	f (Hz)	vs (cm/min)	H (J/mm)
1	350	2	60	8	100	44	400
2	350	2	60	8	100	27	650
3	350	2	60	8	100	25	708
4	350	2	60	8	100	22	805

Considering the welding conditions established, the average current was determined according to Equation 1:

$$I_m = \frac{I_p t_p + I_b t_b}{t_p + t_b} \quad (1)$$

Where t_b is the base time and was derived from Equation 2:

$$t_b = \frac{1}{f} - t_p \quad (2)$$

Where f is the pulsing frequency level.

The heat input (H) was derived from the classical welding Equation 3:

$$H = \frac{I_m V}{v_s} \quad (3)$$

Where V is the voltage level.

These compositions play a crucial role in determining the material properties and behavior during welding processes, making them essential factors in achieving desired welding outcomes, including weldability, mechanical properties, and corrosion resistance.

Table 2 presents the experimental welding conditions used in this study, offering insights into the key parameters applied throughout the welding procedure. The table encompasses data from four distinct experiments, labeled as Experiments 1 through 4. These experiments involve a range of welding parameters, including peak current (I_p) in amperes (A), peak time (t_p) in milliseconds (ms), base current (I_b) in amperes

(A), base time (t_b) in milliseconds (ms), frequency (f) in Hertz (Hz), travel speed (v_s) in centimeters per minute (cm/min), and heat input (H) in joules per millimeter (J/mm). Systematic manipulation of these parameters was performed to explore their impact on the welding process and resulting weld characteristics, facilitating a comprehensive analysis of welding behavior and its correlation with material properties and performance.

After welding, all test specimens underwent machining in accordance with the preparation method outlined in Figure 3 for subsequent Stress Corrosion Cracking (SCC) tests. The sample preparation and test procedures adhered to established standards as outlined by Lundqvist³¹, and in the ASTM E8-79³².

Notably, each specimen featured two 8 mm diameter holes spaced 105 mm apart, center to center. The corrosion tests were conducted under tension using a constant-load-type apparatus, employing tensile test specimens without a V-notch, like those utilized in standard tensile tests.

The experimental setup comprised a device equipped with a system designed to apply a constant force to the test specimen, in the Figure 4. The force was exerted via a fixed weight, transmitted through the movement of a pulley driving a main shaft, which, in turn, moved the lever in a vertical direction along the torsion axis. This rotational motion of the support shaft, counterclockwise, generated a tensile force on the specimen. A digital indicator connected to the control panel recorded this force, measured by a load cell.

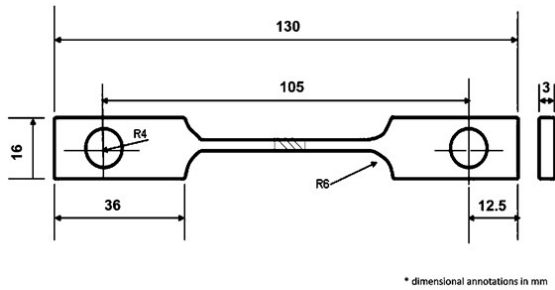


Figure 3. Design of the smooth tensile specimen used in SCC tests.

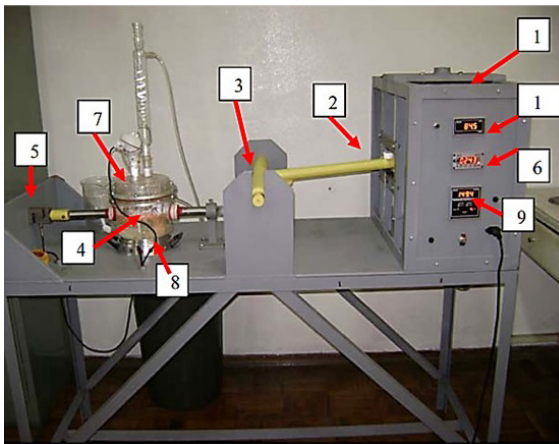


Figure 4. Stress corrosion test device.

As part of the testing procedure, each specimen was immersed in a corrosive solution of magnesium chloride ($MgCl_2$) with a concentration of 43%. The solution was contained within a glass cell heated by an electric heater to maintain a temperature of 145 °C, which was monitored by a digital temperature sensor PT-100 integrated into the control panel. A digital timer recorded the time elapsed until material rupture. The axial tension applied to the specimen's axis equaled 90% of the 0.2% yield strength of the ferritic stainless steel AISI 409.

Following fracture, each specimen was sectioned to obtain a 20mm-length segment for microstructural characterization using optical microscopy and scanning electron microscopy (SEM, Figure 5).

Before being subjected to fractographic analysis, all samples underwent a superficial cleaning process, which consisted of washing the samples several times with isopropyl alcohol with the aid of an ultrasound device. Subsequently, the fracture surfaces of the specimens from the tensile tests and specimens from the CST tests in the medium containing $MgCl_2$ were analyzed³³.

The evaluation of susceptibility to stress corrosion in this study was based on the time of total rupture of the specimens and the applied load.

The ferritoscopy, a non-destructive metallographic technique, is employed to assess ferrite quantity and distribution in microstructures. The ferritoscope, a specialized instrument, utilizes the magnetic induction method for precise measurements of ferrite content in austenitic and duplex steel³⁴. This modern



Figure 5. Scanning electron microscope LEO ZEISS model 1450 VP with Oxford Inca Energy spectrometer.

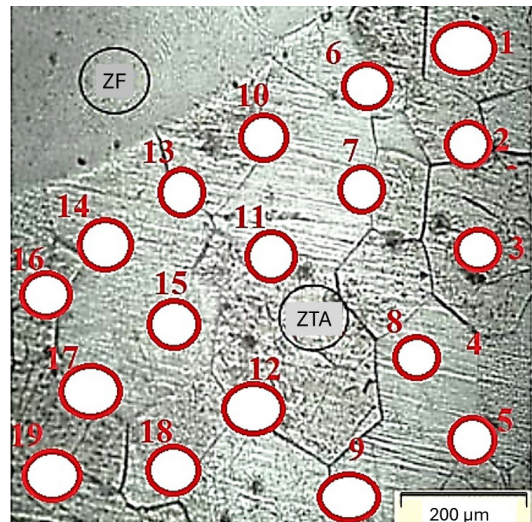


Figure 6. Ferritoscopy points on the HAZ region.

tool is versatile, finding application in austenitic steel sheets, stainless steel welding seams, pipes, containers, boilers, and other products made from austenitic or duplex steel³⁵. For this study, a Fischer model FMP30 digital ferritoscope was calibrated with base ferrite standards ranging from 10.2% to 59.8%. Using a cut sheet as the test specimen, 19 measurements were concentrated on the Heat-Affected Zone (HAZ) region. Notably, readings are instantaneous upon probe placement at the measurement location or continuous until the probe is lifted, as depicted in Figure 6.

3. Results and Discussion

3.1. Microstructure

Figure 7a shows the microstructure of the Heat-Affected Zone (HAZ) subjected to a heat input of 805 J/mm, consisting of polygonal ferrite grains. However, the Figure 7b shows the presence of precipitates rich in titanium and niobium, which are characterized through microanalysis by dispersive energy – EDS.

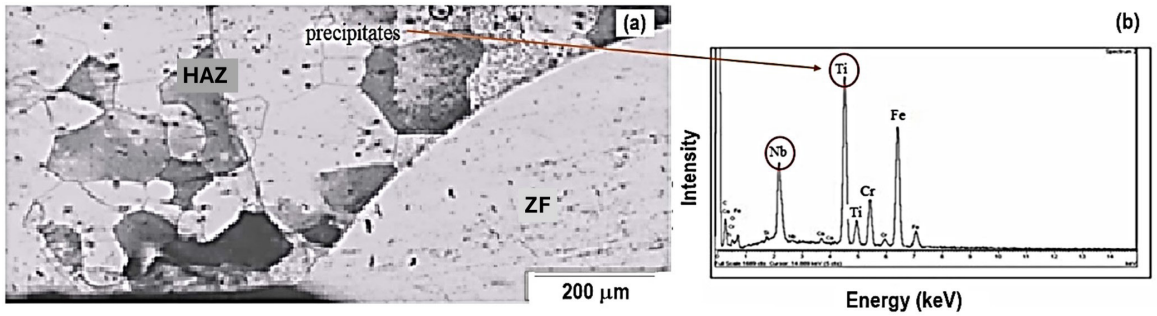


Figure 7. (a) Microstructure of heat affected zone and fusion zone. $H = 805 \text{ J/mm}$. Etching: Reagent Marble, attack time 40s. (b) Energy dispersive micro-analysis of the highlighted region the precipitates.

It is noteworthy that the precipitation in the titanium and niobium introduces compositional heterogeneities along the grain boundaries, rendering these areas anodic in comparison to the remainder of the grains. Furthermore, precipitation further accelerates the development of corrosion cracks and stress concentration points.

Figure 8 presents the microstructure of the weld metal; wherein varying amounts of delta ferrite were evident across the analyzed samples. As summarized in Table 3, the ferrite content ranged from 6.4% to 7.0%, with variations attributed to the distinct heat inputs employed.

In general, both low and high heat input welds exhibited a continuous network of vermicular delta ferrite. Hence, it becomes imperative to exercise precise control over the total delta ferrite content in applications necessitating robust corrosion resistance, high weld toughness at low temperatures, and when any residual magnetism is to be avoided in the final component.

Table 3 presents the results of ferrite content measurements in the Heat-Affected Zone (HAZ) using the ferristocopy test. The data are categorized according to different heat input levels, expressed in joules per millimeter (J/mm). The corresponding delta ferrite percentages are provided alongside their respective uncertainties. At a heat input of 400 J/mm, the delta ferrite content was determined to be 6.4% with an uncertainty of $\pm 0.250\%$. Similarly, for heat inputs of 650 J/mm, 708 J/mm, and 805 J/mm, the delta ferrite percentages were measured at 6.6%, 6.5%, and 7.0%, respectively, each with their corresponding uncertainties. according to Figure 9. These findings offer valuable insights into the variations of ferrite content within the HAZ under different welding conditions, thereby contributing to a comprehensive understanding of the material's microstructure.

In studies concerning Sulfide Stress Corrosion Cracking and Fatigue Crack Growth in welded materials³⁶, it was found that the influence of delta ferrite presence in austenitic welds on susceptibility to stress corrosion cracking is more associated with its shape and distribution within the austenitic matrix rather than its absolute content. However, in the tests that were conducted, it was observed that welds produced with low heat input ($H = 400 \text{ J/mm}$) exhibited a lower delta ferrite content compared to welds created with higher heat input ($H = 805 \text{ J/mm}$). This discrepancy arises from the faster cooling rates experienced by the former joints.

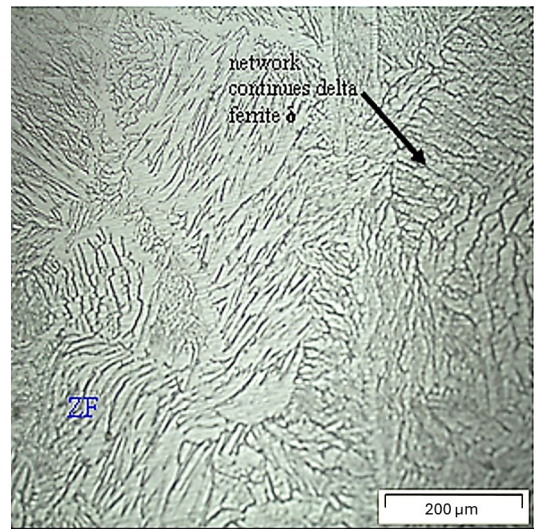


Figure 8. Microstructure of the specimen welded with $H = 400 \text{ J/mm}$. Etching: Electrolytic time 2min and 30s.

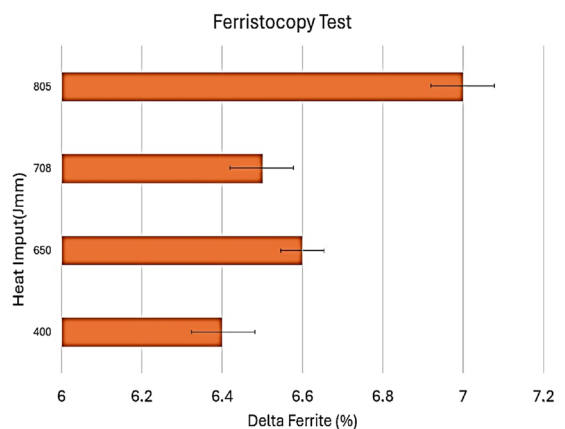


Figure 9. Ferristocopy Test.

Table 3. Measuring the ferrite content in the Heat-Affected Zone (HAZ) using the ferristocopy test.

Heat input(J/mm)	Delta ferrite (%)
400	6.4 +/- 0.3
650	6.6 +/- 0.2
708	6.5 +/- 0.3
805	7.0 +/- 0.3

It is worth emphasizing that precise control of delta ferrite content in stainless steel welds is of paramount importance. An excessive amount of delta ferrite (exceeding 10% by weight) can lead to reduced ductility, mechanical strength, and corrosion resistance. Conversely, when the delta ferrite content is excessively low (less than 5% by weight), the risk of hot cracking during the solidification of the weld metal increases.

3.2. Microhardness

Microhardness within the welded joint can provide insight into various structural changes induced by multiple factors, including the welding thermal cycle, filler metal composition, and the alignment of mechanical properties between the weld metal and the base metal. Notably, the Heat-Affected Zone (HAZ), particularly in the vicinity of the fusion line, tends to experience hardening due to the welding process³⁷.

Figure 5 illustrates the hardness behavior of the welds subjected to different heat inputs. Microhardness measurements were taken horizontally across the sample cross-section at various points using the following designation: points 1, 2, 3, 11, and 12 correspond to the melted bead (Mb), while points 4, 5, 9, and 10 represent the Heat-Affected Zone (HAZ), fused zone correspond to the point 6 and 7.

Upon closer examination of Figure 10, it is evident that welds produced with lower heat input ($H = 400 \text{ J/mm}$) exhibited higher microhardness, in line with our expectations. This can be attributed to their accelerated cooling rates and the presence of specific chemical elements within the weld metal.

Table 4 provides a detailed overview of the variation in average microhardness test results for welding at different heat input levels. The table includes nine data points (labeled as "Points") corresponding to specific test conditions, each associated with four microhardness measurements: d1 ($\text{HV}_{0.2}$), d2 ($\text{HV}_{0.2}$), d3 ($\text{HV}_{0.2}$), and d4 ($\text{HV}_{0.2}$). For each data point, the table displays the mean hardness values and their respective standard deviations (s). Additionally, the heat input levels, expressed in joules per millimeter (J/mm), are listed at the bottom of the table. These comprehensive hardness test results offer valuable insights into the material's mechanical properties under various welding conditions, contributing to a deeper understanding of its behavior and performance.

Table 4 presents the maximum microhardness, which reached 230 HV across all welding conditions. This value aligns with acceptability criteria specified in standards³⁸⁻⁴⁰. These standards prescribe a maximum hardness of 250 HV for materials used in petroleum equipment to mitigate stress corrosion cracking in environments containing H_2S .

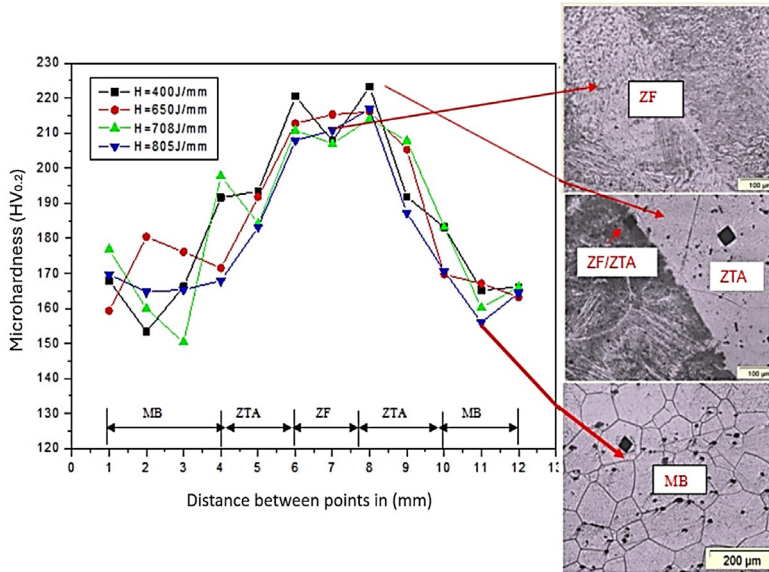


Figure 10. Vickers microhardness and microstructure behavior at the coded points.

Table 4. Variation of the average micro hardness tests for welding.

Points	d1 ($\text{HV}_{0.2}$)	s	d2 ($\text{HV}_{0.2}$)	s	d3 ($\text{HV}_{0.2}$)	s	d4 ($\text{HV}_{0.2}$)	s
1	167.9	2.26	159.3	12.82	176.8	11.88	169.7	11.53
2	191.6	1.20	171.5	8.23	197.8	26.73	167.9	10.36
3	193.4	19.52	191.8	0.85	184.2	4.10	183.2	18.73
4	216.7	1.27	212.8	8.34	207.7	12.52	207.9	12.66
5	220.6	5.56	215.3	22.84	218.6	21.64	210.8	18.24
6	229.7	4.50	216.1	25.53	214.1	24.11	216.9	21.85
7	207.8	3.50	205.3	16.17	191.8	17.54	187.3	15.63
8	183.2	7.92	169.7	19.16	183.2	7.92	170.6	14.07
9	166.1	1.48	163.2	9.10	166.1	2.90	164.4	11.24
Heat input (J/mm)	400		650		780		805	

3.3. Stress corrosion cracking

Table 4 presents the results obtained from the metallographic analysis of specimens subjected to stress corrosion cracking (SCC) tests in a 43% weight/volume magnesium chloride solution. It is evident that the specimens exhibit similar SCC resistance behavior in the presence of chlorides. Notably, an increase in welding heat input correlates with an extended time to rupture in the analyzed samples. This underscores the significant influence of heat input on fracture susceptibility.

Lower heat input usage significantly elevates the risk of fracture, resulting in shorter times to failure. This phenomenon can be attributed to the rapid cooling rates associated with this welding condition, leading to the formation of a microstructure more susceptible to fracture. Conversely, increasing heat input demonstrates a trend towards reducing fracture risk, with a clear stabilization tendency observed at higher heat input levels (708 and 805 J/mm). Nonetheless, additional testing is warranted to bolster this hypothesis.

Table 5 presents the results of stress corrosion cracking (SCC) tests conducted on welded specimens. The Table includes data from eight distinct experiments, each characterized by specific welding conditions. The parameters listed for each experiment encompass the heat input (expressed in J/mm), rupture time (measured in minutes), test temperature (in degrees Celsius), and the region of fracture observed. The regions of fracture are categorized as either "HAZ" (Heat-Affected Zone) or "HAZ/ZF" (Heat-Affected Zone and Fusion

Zone), and the fracture behavior is classified as "Ductile" or "Brittle." These SCC test results provide valuable insights into the material's susceptibility to stress corrosion cracking under different welding conditions, aiding in a comprehensive assessment of its performance and reliability.

It is worth noting that all analyzed samples exhibited complete fractures within the Heat-Affected Zone (HAZ), as shown in Table 5, regardless of the energy input level applied. This observation underscores the HAZ's heightened susceptibility to corrosion-induced cracking. This susceptibility arises from the rapid thermal cycling experienced by this region, leading to metallurgical alterations in its structure, including carbide precipitation, phase formation, and irreversible grain size growth.

The rapid thermal cycling experienced by this region induces substantial alterations in the behavior of the Time to Fracture versus Heat Input curve, as shown in Figure 11. These alterations suggest the occurrence of carbide precipitation, phase transformations, and irreversible grain size growth, collectively increasing the material's susceptibility to stress corrosion cracking (SCC). These comprehensive findings significantly enhance our understanding of material behavior in diverse welding conditions and emphasize the critical importance of precise heat input control in welding processes, ensuring structural integrity and resistance against SCC-induced failures. Further research is essential to explore this relationship more deeply, encompassing a broader spectrum of conditions for a comprehensive understanding.

Table 5. SCC tests results on specimens welding.

Experiments	Heat input (J/mm)	Rupture time (min)	Temperature (°C)	Region	Fracture
1	400	3659	145	HAZ	Ductile brittle
2	400	3639	145	HAZ/ZF	Ductile brittle
3	650	6571	145	HAZ/ZF	Ductile brittle
4	650	7094	145	HAZ	Ductile brittle
5	708	7843	145	HAZ	Ductile brittle
6	708	7931	145	HAZ	Ductile brittle
7	805	6181	145	HAZ/ZF	Ductile brittle
8	805	7778	145	HAZ	Ductile brittle

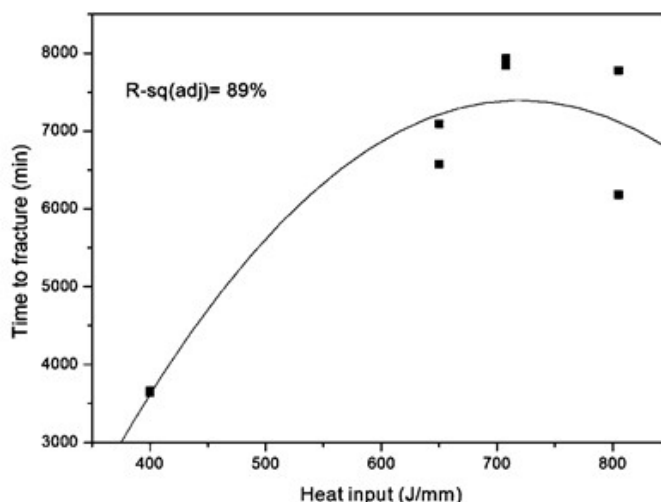


Figure 11. Influence of the heat input on the time to fracture.

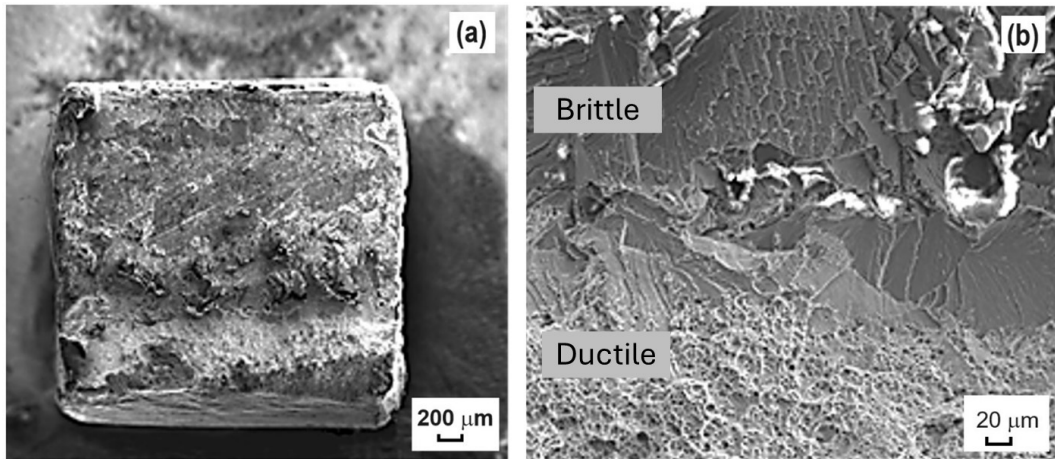


Figure 12. Characterization of the ductile-brittle fracture transition at $H= 650 \text{ J/mm}$.

3.4. Fractography

Microscopic analysis of the fractured region, as shown in Figure 12a and Figure 12b, revealed the presence of two distinct regions: one resulting from the corrosion process and the other attributed to fracture mechanisms induced by increased tensile stresses arising from specimen reduction. Notably, the samples exhibited a region with a ductile-fragile appearance.

Furthermore, the presence of dimples emphasized the ductile nature of the fracture. Scanning electron microscopy (SEM) images highlighted the brittle aspect of the fracture, characterized by facet cleavage, suggesting that stress corrosion cracking (SCC) played a significant role in the material's fracture.

Analysis of crack morphology through metallographic examinations reveals that the crack propagated within the interior of grains, exhibiting a transgranular fracture type with multiple branches, as illustrated in Figure 13. Crack propagation consistently occurred perpendicular to the applied force direction, and no evidence of intergranular fracture due to stress corrosion cracking (SCC) was observed.

A more comprehensive analysis of the cracked region was conducted using scanning electron microscopy (SEM), as shown in Figure 14. It is evident that numerous microcracks are present, localized at the grain boundaries within the Heat-Affected Zone (HAZ) region. These findings suggest that the deposited weld metal, originating from a tubular austenitic wire, has led to a reduction in resistance to cracking induced by stress corrosion cracking (SCC).

4. Conclusions

In summary, the study has yielded the following key observations:

- Welds generated with reduced heat input have exhibited an inclination towards increased hardness within the Heat-Affected Zone (HAZ). This phenomenon primarily arises from carbide precipitation along the grain boundaries of the ferrite phase. This precipitation is a contributing factor to decreased resistance against stress corrosion

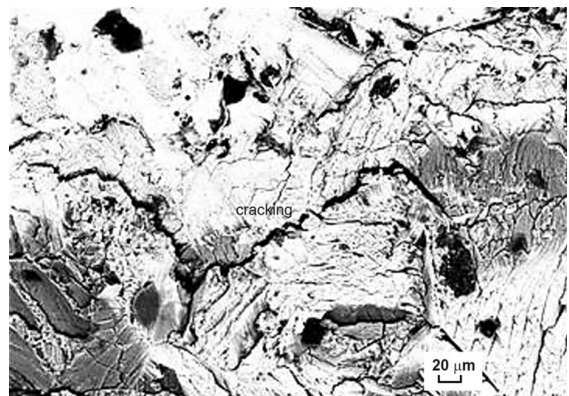


Figure 13. Transgranular cracking of SCC in the region of HAZ, $H = 650 \text{ J/mm}$. Etching electrolytic.

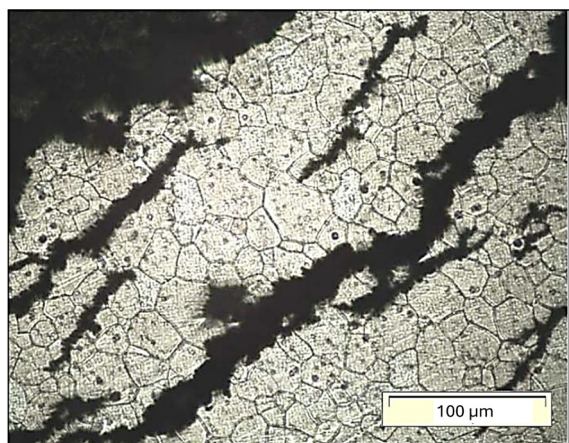


Figure 14. Transgranular and intergranular Microcracks in the region of HAZ, $H = 400 \text{ J/mm}$. Attack: electrolytic, attack time 2.5 minutes.

cracking (SCC). The carbide-enriched regions along the grain boundaries tend to become anodic relative to the surrounding material, thereby promoting the mechanism of anodic dissolution, leading to SCC-induced cracking.

- Conversely, welds produced with the highest heat input have demonstrated heightened resistance to stress corrosion cracking. However, it is essential to note that the slight variation in heat input values employed in this study cautions against making over-generalizations regarding this outcome.
- In-depth analysis of crack morphology through metallography has revealed transgranular fractures characterized by numerous branching patterns. These fractures initiated in the weld metal, primarily composed of austenitic material, and subsequently extended into the ferritic base metal.

These findings collectively underscore the intricate relationship between heat input, material characteristics, and susceptibility to SCC within welded joints. They emphasize the necessity for nuanced assessments when evaluating the performance and reliability of welds.

5. Acknowledgments

The authors are grateful to Arcelor Mittal Inox for providing the material and to CNPq and FAPEMIG for the financial support to this project.

6. References

1. Zhou W. Stress corrosion cracking causes and solutions. Singapore: Singapore Welding Society; 1998. p. 1-6. Newsletter.
2. Brown BF. The application of fracture mechanics to stress-corrosion cracking. *Metall Rev.* 1968;13(1):171-83.
3. Lynch SP. Effect of environment on fracture-mechanisms of liquid metal embrittlement, stress corrosion cracking and corrosion-fatigue. In: ICF4; 1977; Waterloo, Canada. Proceedings. Cassino, Italy: ESIS Publishing House; 1977.
4. Bauernfeind D, Romotowski J, Haberl J, Mori G, Bernauer J, Saller G. Stress corrosion cracking of highly alloyed austenitic stainless steel in chloride media. Austria: University of Leoben; 2004. p. 1-8.
5. Alyousif OM, Nishimura R. The effect of test temperature on SCC behavior of austenitic stainless steel in boiling saturated magnesium chloride solution. *Corros Sci.* 2006;48:4283-93.
6. Chen YY, Liou YM, Shih HC. Stress corrosion cracking of type 321 stainless steels in simulated petrochemical process environments containing hydrogen sulfide and chloride. *Mater Sci Eng A.* 2005;407(1-2):114-26.
7. Zannotto F, Grassi V, Balbo A, Monticelli C, Zucchi F. Stress corrosion cracking of LDX 2101® duplex stainless steel in chloride solutions in the presence of thiosulphate. *Corros Sci.* 2014;80:205-12.
8. Taban E, Kaluc E. Plasma arc welding of AISI316Ti (EN 1.4571) stainless steel: mechanical, microstructural, corrosion aspects. *Mater Test.* 2014;56(4):294-9.
9. Bahadori A. Corrosion and materials selection: a guide for the chemical and petroleum industries. New York: John Wiley & Sons; 2014.
10. Gertsman VY, Bruemmer SM. Study of grain boundary character along intergranular stress corrosion crack paths in austenitic alloys. *Acta Mater.* 2001;49(9):1589-98.
11. van Boven GV, Chen W, Rogge R. The role of residual stress in neutral pH stress corrosion cracking of pipeline steels-part i: pitting and cracking occurrence. *Acta Mater.* 2007;55(1):29-42.
12. Cheng YF. Stress corrosion cracking of pipelines. New York: John Wiley & Sons; 2013.
13. Egbewande A, Chen W, Eadie R, Kania R, van Boven G, Worthingham R, et al. Surface crack growth behavior of pipeline steel under disbonded coating at free corrosion potential in near-neutral pH soil environments. *Metall Mater Trans, A Phys Metall Mater Sci.* 2014;45(11):4946-59.
14. Sui G, Charles EA, Congleton J. The effect of delta-ferrite content on the stress corrosion cracking of austenitic stainless steels in a sulphate solution. *Corros Sci.* 1996;38(5):687-703.
15. Henke SL, Paredes RSC, Capra AR. Development of delta ferrite on the weld and HAZ produced by pulsed plasma arc welding on a supermartensitic stainless steel. *Welding International.* 2014;29(4):285-90.
16. Ahmed II, Fonseca JQ, Sherry AH. Effect of strain paths and residual delta ferrite on the failure of cold rolled austenitic stainless steels, type 304L. *J Strain Anal Eng Des.* 2013;48(7):410-9.
17. Ortiz N, Curiel FF, López VH, Ruiz A. Evaluation of the intergranular corrosion susceptibility of UNS S31803 duplex stainless steel with thermoelectric power measurements. *Corros Sci.* 2013;69:236-44.
18. Modenesi PJ. Soldabilidade dos aços inoxidáveis. São Paulo: SENAI-SP; 2001. 100 p. (Coleção Tecnologia da Soldagem; 1).
19. Gomes AJM, Jorge JCF, Souza LFG, Bott IS. Influence of chemical composition and post welding heat treatment on the microstructure and mechanical properties of high strength steel weld metals. *Mater Sci Forum.* 2013;758:21-32.
20. Mas F, Tassin C, Kozeschnik E, Roch F, Todeschini P, Brechet Y. Microstructures formation and phase transformations around the interface of welds between dissimilar steels. *MATEC Web Conf.* 2013;7:02001.
21. Jeong HS, Lee YY, Bae DS. The effect of alloying elements on weldability and corrosion resistance of austenitic stainless steels (I). *J Korean Weld Joining Soc.* 2012;30(3):57-65. <http://doi.org/10.5781/KWJS.2012.30.3.255>.
22. Lopes AS, Colosio M, Castillo J. Technological comparison for dual phase and advanced high strength low alloy steels regarding weldability and mechanical properties. Warrendale: SAE International; 2014. (SAE Technical Paper; 2014-01-0988).
23. Vieira DHP, Carvalho DF, Bálamo PSS, Godefroid LB, Cândido LC. Comportamento em corrosão de juntas soldadas de aços inoxidáveis em meios contendo íons cloretos. *Tecnol Metalurgia Materiais.* 2006;3(2):6-10.
24. Souza CS, Lins VDFC, Silveira DMD, Costa CGF, Cardoso R Jr, Campos FR, et al. Evaluation of multipass welding of thick lean duplex stainless steel UNS S32304 plates welded by SMAW, GMAW and FCAW-: corrosion resistance. *Soldag Insp.* 2013;18(3):257-67.
25. Lopes AS, Colosio M, Castillo J. Welding metallurgy and weldability of stainless steels. New York: John Willey & Sons; 2005.
26. Hajiannia I, Shamanian M, Kasiri M. The weldability evaluation of dissimilar welds of AISI 347 stainless steel to ASTM A335 low alloy steel by gastungesten arc welding. *J Adv Mater Process.* 2013;1(4):33-40.
27. Sundaresan S. Metallurgy of welding stainless steels. *Adv Mat Res.* 2013;794:274-88.
28. Folkhard E. Welding metallurgy of stainless steels. New York: Springer; 1998.
29. Kurt Hİ, Samur R. Study on microstructure, tensile test and hardness 304 stainless steel jointed by TIG welding. *Int J Sci Technol.* 2013;2(2):163-8.
30. Dias AO. Análise da influência dos parâmetros de pulsação na soldagem do aço inoxidável AISI 304 através do arame tubular AWS E316LT1-4 [dissertação]. Itajubá: Universidade Federal de Itajubá; 2009. 116 p.
31. Lundqvist B. Soldagem dos aços inoxidáveis nas indústrias de celulose e papel. *Soldas e Eletrodos; junho 1977.* p. 8-18.
32. ASTM: American Society for Testing and Materials. ASTM E8-79: standard methods of tension testing of metallic materials. West Conshohocken: ASTM; 1985.

33. ASTM: American Society for Testing and Materials. ASTM G58-78: standard practice for the preparation of stress corrosion test specimens for weldments. West Conshohocken: ASTM; 2005.
34. Marques AVM, Carmo KMD, Lage WC, Teixeira RLP, Lacerda JCD, Teixeira CHSB, et al. Evaluation of the effect of plastic deformation on the microstructure, hardness and magnetic properties of AISI type 316L stainless steel. *Materia*. 2020;25:e-12611.
35. Teixeira RLP, Lacerda JC, Florencio KC, Silva SN, Henriques AB. TRIP effect produced by cold rolling of austenitic stainless steel AISI 316L. *J Mater Sci*. 2023;58(7):3334-45.
36. Mashhuriazar A, Gur CH, Sajuri Z, Omidvar H. Effects of heat input on metallurgical behavior in HAZ of multi-pass and multi-layer welded IN-939 superalloy. *J Mater Res Technol*. 2021;15:1590-603.
37. Tsay LW, Chen YC, Chan SLI. Sulfide stress corrosion cracking and fatigue crack growth of welded TMCPAPI 5LX65 pipe-line steel. *Int J Fatigue*. 2001;23(2):103-13.
38. Kumar A, Pacheco JL, Desai SK, Huang W, Reddy RV, Sun W, et al. Selecting representative laboratory test conditions for mildly sour Sulfide Stress Corrosion (SSC) testing. In: *CORROSION 2014; 2014*; San Antonio, Texas, USA. Proceedings. Richardson, TX: OnePetro; 2014.
39. Cheng YF. *Stress corrosion cracking of pipelines*. New York: John Wiley & Sons; 2013.
40. NACE International. *NACE MR0175: petroleum and natural gas industries materials for use in H₂S-containing environments in oil and gas production*. 1st ed. New York: The Corrosion Society; 2001. 144 p.